RESEARCH ARTICLE

Key Points:
- We characterize high-latitude irregularities using GPS data, SIGMA model, and an inverse method
- Phase scintillations as high rate GPS data at multiple polar locations across the Arctic and Antarctic are both measured and modeled
- Spectral indices we found for F region irregularities are as expected for 3-D spectra indicated that inverse modeling approach is valid

Correspondence to:
K. B. Deshpande,
kbdeshpande@gmail.com

Satellite-beacon Ionospheric-scintillation Global Model of the upper Atmosphere (SIGMA) II: Inverse modeling with high-latitude observations to deduce irregularity physics

K. B. Deshpande[1,2], G. S. Bust[3], C. R. Clauer[1], W. A. Scales[1], N. A. Frissell[1], J. M. Ruohoniemi[1], L. Spogli[4,5], C. Mitchell[6], and A. T. Weatherwax[7]

[1]Bradley Department of Electrical and Computer Engineering, Virginia Tech, Blacksburg, Virginia, USA, [2]Now at Department of Physical Sciences, Embry-Riddle Aeronautical University, Daytona Beach, Florida, USA, [3]The Johns Hopkins University Applied Physics Laboratory, Laurel, Maryland, USA, [4]Istituto Nazionale di Geofisica e Vulcanologia, Rome, Italy, [5]SpacEarth Technology, Rome, Italy, [6]Department of Electronic and Electrical Engineering, University of Bath, Bath, UK, [7]Merrimack College, North Andover, Massachusetts, USA

Abstract Ionospheric scintillation is caused by irregularities in the ionospheric electron density. The characterization of ionospheric irregularities is important to further our understanding of the underlying physics. Our goal is to characterize the intermediate (0.1–10 km) to medium (10–100 km) scale high-latitude irregularities which are likely to produce these scintillations. In this paper, we characterize irregularities observed by Global Navigation Satellite System (GNSS) during a geomagnetically active period on 9 March 2012. For this purpose, along with the measurements, we are using the recently developed model: "Satellite-beacon Ionospheric-scintillation Global Model of the upper Atmosphere" (SIGMA). The model is particularly applicable at high latitudes as it accounts for the complicated geometry of the magnetic field lines in these regions and is presented in an earlier paper. We use an inverse modeling technique to derive irregularity parameters by comparing the high rate (50 Hz) GNSS observations to the modeled outputs. In this investigation, we consider experimental observations from both the northern and southern high latitudes. The results include predominance of phase scintillations compared to amplitude scintillations that imply the presence of larger-scale irregularities of sizes above the Fresnel scale at GPS frequencies, and the spectral index ranges from 2.4 to 4.2 and the RMS number density ranges from 3e11 to 2.3e12 el/m^3. The best fits we obtained from our inverse method that considers only weak scattering mostly agree with the observations. Finally, we suggest some improvements in order to facilitate the possibility of accomplishing a unique solution to such inverse problems.

1. Introduction and Motivation

Ionospheric scintillations in Global Navigation Satellite System (GNSS) signals are rapid variations in their amplitude and phase resulting from electron density irregularities in the ionosphere. Scintillations are frequently observed in high-latitude and equatorial regions [*Aarons*, 1982; *Kintner et al.*, 2009]. It has been shown that in the dayside auroral region, large-scale phase scintillations are observed more often than amplitude scintillations [*Aarons*, 1997; *Basu et al.*, 1998]. More recent observations reported by *Mitchell et al.* [2005] and statistical work by *Spogli et al.* [2009] in the northern high-latitude regions and by *Kinrade et al.* [2012] and *Deshpande et al.* [2012] in the southern high-latitude regions also indicated a predominance of phase scintillations. Statistical results from the South Pole presented by *Kinrade et al.* [2013] emphasize the occurrence of Global Positioning System (GPS) phase scintillations coexisting with auroral emissions. *Alfonsi et al.* [2011] describe the scintillation climatology of the high-latitude ionosphere over both the poles and also highlight the difference between amplitude and phase scintillations.

Our goal is to characterize the intermediate (0.1–10 km) scale to medium scale (10–100 km) [*Kelley et al.*, 1982a] high-latitude irregularities which are likely to produce these phase scintillations. This is a step toward our goal of understanding the underlying mechanisms that produce the density irregularities and their relationship to magnetospheric-ionospheric coupling. In this paper, we propose a way to characterize the irregularities, by using the GNSS scintillation observations and observations from other ancillary

instruments coupled with the physical and propagation parameters derived from the model: "Satellite-beacon Ionospheric-scintillation Global Model of the upper Atmosphere" (SIGMA) [*Deshpande et al.*, 2014]. The parameters derived from the auxiliary instruments together with the inverse method using SIGMA can be used to extract the physical characteristics of the irregularities involved in the generation of the scintillations.

A few good examples of the inverse modeling technique can be found in the works of *Keskinen* [2006] and *Carrano et al.* [2012], where they use the technique to infer turbulence parameters from intensity scintillation data obtained at low-latitude regions. Although the iterative parameter estimation technique presented by *Carrano et al.* [2012] is similar to our inverse modeling methodology, the latitudes they consider, their underlying model, and the free parameters they fit are different. Moreover, we are utilizing 50 Hz phase scintillation observations, whereas they worked with 10 Hz GPS carrier-to-noise measurements.

Additionally, low-rate scintillation indices S4 and σ_ϕ have been used in interhemispheric studies [*Prikryl et al.*, 2010, 2011, 2012, 2015]. However, to our knowledge, the morphology and geographical distribution of intermediate- and medium-scale irregularities at high latitudes has not been explored with high-rate (typically 50 Hz) scintillation data along with modeling.

The organization of this paper is as follows: we provide details on the observations as well as briefly discuss SIGMA in section 2. In section 3, we describe our inverse modeling methodology. We present our results from inverse modeling and discuss them in section 4. Finally, we conclude our findings and discuss our future plans in section 5.

2. Data Sets and Model

2.1. GPS and Auxiliary Data Sets

During the period of 7 to 17 March 2012 there occurred a series of very active geomagnetic storms and substorms [*Prikryl et al.*, 2015]. We select 9 March 2012 for analysis based on the strength of geomagnetic activity along with the availability of coexisting auxiliary observations and good scintillation measurements. This day gives us an opportunity to explore the high-latitude irregularity physics during storm conditions at different geographical locations. For this paper, we focussed on six different locations, three from each hemisphere. In the Northern Hemisphere, we have high-rate (50 Hz) GPS scintillation data from receivers at Ny-Ålesund (NY0), Tromsø, and Resolute Bay (ResBay), and in the Southern Hemisphere, we have scintillation data from receivers at McMurdo (MCM), South Pole (SPA), and Concordia (DMC0). We list the geographic and geomagnetic coordinates of these stations in Table 1.

A preliminary examination of low-rate S4 and σ_ϕ data revealed the possible times and dates during the March 2012 period mentioned above. Results from a detailed search for scintillation observations and supporting measurements from ancillary instruments such as the Super Dual Auroral Radar Network (SuperDARN) and incoherent scatter radar (ISR) motivated us to select the interval from 3 to 4 UT on 9 March 2012. *Kp* index was 6 during this time, and it was the beginning of a geomagnetic storm. Moreover, this time period reveals continuous periods of phase scintillations greater than 30 s in duration on most of the receivers. This is an important factor in our inverse modeling since we need to have at least 30 s of continuous scintillations in order to compare with a simulated phase time series of the same duration.

During the period of interest, we did not observe power fluctuations greater than the noise floor in the GPS high-rate data at any of the locations. The noise floor was found from the nonscintillating times during 3 to 4 UT on 9 March 2012 for each location and was to maximize at ±2 dB. This is consistent with the prevalence of phase scintillations observed at high latitudes as discussed in section 1. Stacked plots of detrended and filtered high-rate GPS phase data at each location during 3 to 4 UT on 9 March 2012 are shown in Figure 1. The latitude is shown on the vertical axis. Black rectangles indicate the scintillation periods from which we have selected 30 s long GPS data used here in the inverse modeling problems. A scale on the right side of the plot represents 3 rad of phase. During this period, we did not observe any scintillations at Concordia which is close to the geomagnetic South Pole. This is an interesting finding that helps place the dynamics of the ionospheric structures within the context of geomagnetic location.

The Canadian High Arctic Ionospheric Network (CHAIN) provided GPS scintillation data for Resolute Bay [*Jayachandran et al.*, 2009]. The electronic Space Weather upper atmosphere site (http://www.eswua.ingv.it/), managed by Istituto Nazionale di Geofisica e Vulcanologia (INGV), provided GPS scintillation data for Concordia and for Ny-Å lesund [*Romano et al.*, 2008, 2013]. Auxiliary data were obtained from the ISR at

Table 1. Geographic and Geomagnetic Coordinates of the Locations Under Study

Location	Symbol	Owner	Geographic (Latitude, Longitude)	Geomagnetic (Latitude, Longitude)
Resolute Bay	ResBay	CHAIN	(74.4°N, 94.5°W)	(82.7°N, 35°W)
Ny-Ålesund	NYA0	INGV	(78.9°N, 11.9°E)	(76.4°N, 109.4°E)
Tromsø	Tromsø	BATH	(69.3°N, 19.1°E)	(66.7°N, 102.1°E)
South Pole	SPA	BATH	(90°S, 97.5°W)	(74.3°S, 18.7°E)
McMurdo	MCM	BATH	(77.8°S, 166.7°E)	(80°S, 33.9°W)
Concordia	DMC0	INGV	(75.1°S, 123.2°E)	(89°S, 59.2°E)

Tromsø, a riometer at South Pole, Defense Meteorological Satellite Program (DMSP) and Polar-orbiting Operational Environmental Satellite (POES), and SuperDARN radars in both hemispheres. We use auroral oval observations from Special Sensor Ultraviolet Spectrographic Imager (SSUSI) instrument on the DMSP satellites http://ssusi.jhuapl.edu/ [*Paxton et al.*, 2002; *Zhang and Paxton*, 2008] and OVATION Prime plots based on the POES data [*Newell et al.*, 2009, 2010; *Machol et al.*, 2012]. The details of how OVATION Prime plots are produced by National Oceanic and Atmospheric Administration (NOAA) can be found at the National Geophysical Data Center website: http://www.ngdc.noaa.gov/stp/ovation_prime/. In section 4 we will refer to these auxiliary data during the discussion of the results from the individual inverse modeling cases.

2.2. SIGMA

SIGMA is a full, three-dimensional (3-D) electromagnetic (EM) wave propagation model which we developed to simulate the propagation of a signal from a moving satellite to the ground through multiple phase screens (MPS). A detailed description of SIGMA can be found in the earlier paper [*Deshpande et al.*, 2014] (SIGMA I paper). Inside SIGMA, we first obtain a spatial electron number density distribution from a spectral model for high-latitude irregularities and then utilize a hybrid method that combines the MPS technique with a split-step solution to the forward propagation equation [*Rino*, 2010; *Rino and Carrano*, 2011], to propagate the signal to
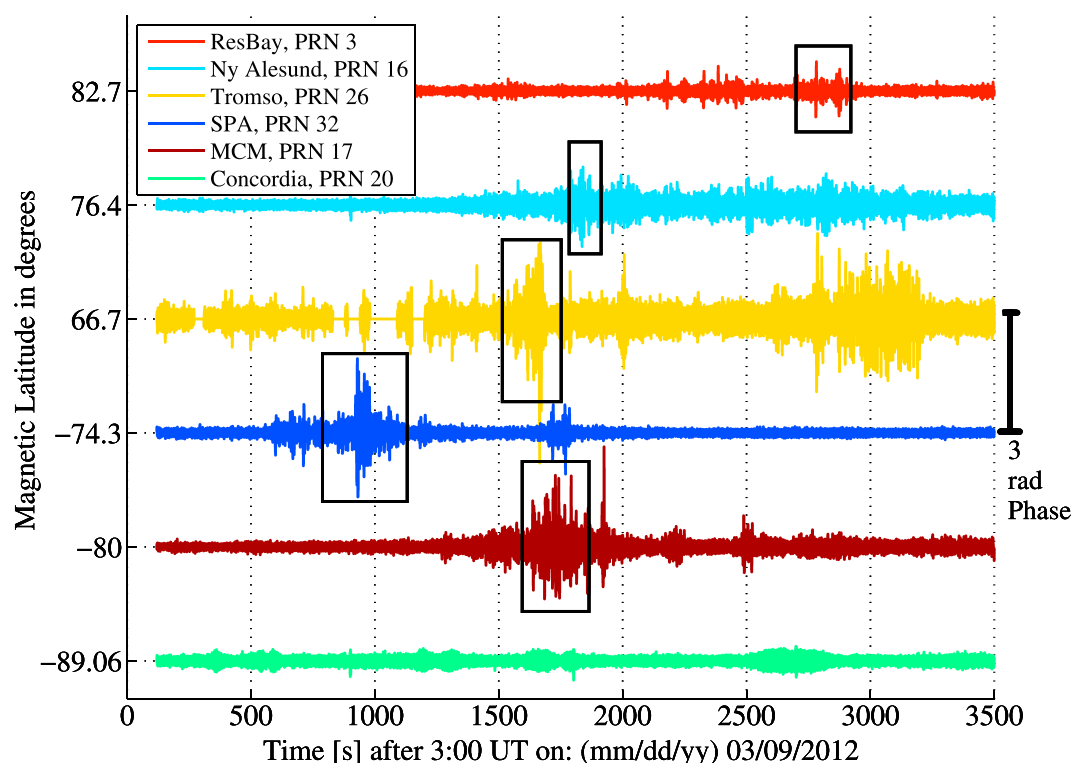

Figure 1. Stacked plots of the phase of GPS signal in radians at six different locations. The vertical scale on the right corresponds to a phase of 3 rad and is included to illustrate the strength of the phase scintillations.

the ground. In this study, we use the Hybrid spectral model of irregularities at high latitudes from *Costa and Kelley* [1977], as described in the SIGMA I paper.

SIGMA outputs high-rate GPS scintillation phase and power time series with 50 Hz sampling frequency. The observed as well as modeled high-rate phase and power are detrended and filtered in order to eliminate any low-frequency effects including the satellite motion. Because the phase scintillations appear more dominant than amplitude scintillations in these high-latitude observations, we are mainly using the simulated phase from SIGMA for the inverse analysis. Comparison of two time series (observed and simulated) can be imprecise since it is not easy to get both of them in-phase to begin with. On the other hand, when comparing the power spectral densities (PSD) of the time series, it is not required to know the relative phases of the complex signals. Thus, in our inverse modeling problems, it is prudent to use PSDs for the comparison of observed and simulated phase.

At 50 Hz sampling frequency, it takes a few hundred seconds for SIGMA to generate a time series as short as 30 s long using a fairly fast single-core processor ($\approx$3 GHz, 8 GB RAM), which therefore results in several hours of run time for an inverse modeling uniform-grid simulation that requires thousands of such runs. These SIGMA runs are performed in parallel several thousand times with different combinations of input parameters. The longer the time series to be simulated by SIGMA, the longer will be the computational time. This constraint limits the length of the SIGMA time series to be 30 s long. This short time length selection also worked positively while we searched for continuous periods of phase scintillations observed at the different locations. For example, the scintillations at NYA0 were not strong, so it was hard to find a continuous chunk of time series longer than 30 s. Once we have the 30 s long phase time series, we obtain its temporal PSD using Welch's method [*Welch*, 1967]. We first divide the time series into 10 s long segments with a 50% overlap, find their individual periodogram values from fast Fourier transforms, and then average them to reduce the noise in the final PSD. In this PSD, since the sampling frequency in the simulated time series is 50 Hz, the Nyquist frequency and thus the maximum frequency is 25 Hz. Furthermore, as the phase time series is originally filtered with a 0.1 Hz high-pass filter to eliminate low-frequency effects as suggested by *Van Dierendonck et al.* [1993], the minimum frequency in the PSD needs to be $\geq$ 0.1 Hz.

3. Method of Inverse Modeling

In this section, we describe the inverse modeling technique we use to fit SIGMA output to the observations and obtain the optimal values of SIGMA input parameters for the best fit. Table 2 presents the input parameters to SIGMA. For a given inverse modeling run, there are eight unknown input parameters (including magnitude $|\mathbf{v}_d|$ and direction $\angle\mathbf{v}_d$ of the drift velocity $\mathbf{v}_d$), which are shown in boldface. These unknowns are found with two steps in the inverse modeling technique as described below. For each observation, the geographical parameters, namely, magnetic dip angle at the receiver location and azimuth and elevation of the vector between the receiver and satellite locations, are obtained beforehand. For the purposes of achieving a realistically possible computation time for inverse modeling problems, we assume a single phase screen.

Initially, for a given GNSS observation, we use the auxiliary data to estimate values of as many input parameters for SIGMA as we can. This is discussed in section 3.1. To reduce the dimension of the design space further, we assume certain values for some of the input parameters, namely, the outer scale, axial ratio, and thickness. The outer scale is the largest spatial dimension of the ionospheric irregularities, while the axial ratio (AXR) is a parameter that defines the anisotropy of the rod-shaped field-aligned irregularities. As described in section 3.2, we retrieve the remaining input parameters for the best fit of the simulated PSD to the observed PSD by running SIGMA over a uniform four-dimensional (4-D) grid that defines a design space.

The turbulence strength is defined by the product of the RMS of the electron number density fluctuations ΔN in electrons/m^3 (el/m^3) and the thickness of the irregularity L_{Th}. It is generally represented in total electron content units (TECU, 1 TECU = 10^{16} el m^{-2}). The magnitude of the PSD in decibel for all frequencies appears to be directly proportional to this turbulence strength [*Rino and Fremouw*, 1977; *Wernik et al.*, 2007; *Deshpande et al.*, 2014]. The magnitude of the effective drift velocity $|\mathbf{v}_d|$ is also expected to affect the strength of the phase as a function of frequency. Finally, we expect *SpInd* to change the shape of the PSD. Therefore, we try to optimize the SIGMA PSD to match the observed PSD, with ΔN (maintaining a constant L_{Th}), *SpInd*, and drift velocity magnitude and direction as the four free parameters.

Table 2. SIGMA Input Parameters[a]

Irregularity	Spectrum Parameters
l_0	**Outer scale** (15 km)
SpInd	**Spectral index** (Step 2)
ΔN	**Root-mean-square (RMS)**
	Electron density fluctuation
	(Step 1 or 2)
AXR	**Axial ratio** (10)
Geographical	Parameters
I	Dip angle (Receiver Location)
LOS(Elv,Az)	LOS vector elevation and azimuth
	between receiver and satellite location
Propagation	Parameters
H_{iono}	**Altitude** (Step 1 or 2)
N_l	Number of layers (1)
L_{Th}	**Thickness** (10 km)
$\mathbf{v}_d$ ($|\mathbf{v}_d|$, $\angle\mathbf{v}_d$)	**Plasma drift velocity** (Step 1 or 2)

[a]The respective steps of the inverse modeling which are used to obtain the input parameters are mentioned in parentheses.

3.1. Step 1: Use of Auxiliary Data

The RMS density ΔN, approximate drift velocity of the ionospheric structures ($|\mathbf{v}_d|$, $\angle\mathbf{v}_d$) and height H_{iono} of the irregularities can be estimated from ISRs. SuperDARN fitted velocity maps can be used to obtain a reasonable estimate of the magnitude and direction of the drift velocities. The magnitude of the velocity can also be approximated from the PSD of the observed intensity. For example, if the PSD of intensity shows a roll over at a frequency f_{roll}, an approximate magnitude of the drift velocity at altitude H_{iono} would be $f_{roll}\sqrt{\lambda H_{iono}}$, where λ is the wavelength of the GPS signal and $\sqrt{\lambda H_{iono}}$ is the Fresnel scale at that altitude. Additionally, the availability of DMSP and POES satellite passes over the regions of interest can indicate the possibility of energetic particle precipitation and can help with auroral oval boundary prediction. If there is auroral precipitation, the ionospheric scintillations are more likely to be from irregularities in the E region or near 120 km. GPS scintillations can also be caused by F region events such as polar cap patches at a typical height of 350 km. The presence of such patches can be validated from either SuperDARN or ISR data or from tomography algorithms such as Ionospheric Data Assimilation Four-Dimensional (IDA4D) [*Bust et al.*, 2004; *Bust and Datta-Barua*, 2014]. On a separate note, electron number densities from data assimilation techniques and tomography algorithms such as IDA4D and Multi-Instrument Data Assimilation System [*Spencer and Mitchell*, 2007] can also be integrated in SIGMA. However, this will be left for future work.

With or without estimates of $|\mathbf{v}_d|$, $\angle\mathbf{v}_d$, and ΔN from auxiliary data, we proceed to step 2 of the method. Furthermore, if, due to absence of auxiliary observations, we cannot estimate the height H_{iono} of the ionosphere with confidence, we implement the inverse modeling technique at both E (120 km) and F (350 km) region altitudes.

The sensitivity study by *Deshpande et al.* [2014] revealed that for axial ratios lower than 5, the two-dimensional (2-D) phase structures on ground look more isotropic, while for values above 30, the coherence length along the z axis becomes larger than the thickness of the layer (10 km). Thus, assuming we have rod shaped irregularities, we consider an axial ratio of 10 and irregularity thickness of 10 km for our simulation. We choose a higher value of outer scale l_0 of 15 km based on the findings of *Rino* [1979], where he found no evidences of a finite l_0 cutoff.

3.2. Step 2: Uniform-Grid SIGMA Simulation

From step 1, we obtain an estimate of four of the eight unknown SIGMA input parameters, namely, H_{iono}, $|\mathbf{v}_d|$, $\angle\mathbf{v}_d$, and ΔN. As mentioned earlier, if H_{iono} is not known, the following analysis is simply run at two different heights. In this section, we describe the method to obtain the best fit values for the four design variables stated earlier, specifically, spectral index, $|\mathbf{v}_d|$, $\angle\mathbf{v}_d$, and ΔN. In the case of three or more design variables, the

inverse modeling problem is a complicated multidimensional problem and will require more sophisticated computational resources if the problem is to be solved using optimization algorithms. In this paper, we solve the problem with four design variables using a simulation performed over a uniformly sampled 4-D grid. Finding and using a multidimensional global optimization algorithm to solve the inverse modeling problem will be considered in subsequent studies.

We incorporate a least squares or chi-square fitting test [*Chernoff and Lehmann*, 1954; *Press et al.*, 1992] to obtain the best fit of the simulated data to the observed data. As explained below, we obtain χ^2 metric for each SIGMA simulation run on the 4-D uniform grid, where SIGMA is executed with a set of different values for the four design variables. In each case, we try to fit the phase PSD of the model to the data in the log-log domain. χ^2 is the least squares fit value and is given by

$$\chi^2 = \frac{1}{\sigma_y^2} \sum_{i=1}^{N} \left(\log_{10} Y_i - \log_{10} X_i \right)^2 \tag{1}$$

where Y_is are N number of points on the PSD of the observed phase, X_is are the points on PSD of the SIGMA phase, and σ_y^2 is the variance on the observed PSD after removal of any trend in the PSD. σ_y^2 represents a constant measurement error on the observed data. We consider a constant error in the χ^2 minimization since the variance on each Y_i point, and thus, the uncertainties associated with the set of GPS measurements are not known in advance.

For a good fit, $\chi^2 \approx (N - M)$ or $\chi' = \chi^2/(N - M) \approx 1$, where $(N - M)$ is the number of degrees of freedom. M is the total number of design variables to be fitted. Furthermore, the PSD values to fit are between f_{min} and f_{max}, where $f_{min} = 0.2$ Hz is the minimum frequency after the filtering of the phase time series and finding the PSD using the Welch's method. We purposefully consider a slightly higher frequency than the filter frequency of 0.1 Hz to avoid interference of any filter artifacts while fitting. f_{max} is the maximum frequency before the noise floor starts. We found it to be around 8.5 Hz. In the current study, N is equal to 83, and M is equal to 4. Thus, $(N-M)$ in this case is 79. In all the results in section 4, the "goodness" of the fit will be higher if the χ^2 value is close to 79 or χ' is close to 1. In other words, the fit is better if $\chi' \approx 1$.

We added another constraint while minimizing this χ' value. Although for all the cases, phase scintillations were predominant, we did not want to exclude intensity variations. Hence, while fitting the phase SIGMA PSD to the observed phase PSD, we selected only those cases for which the peak to peak variation of the simulated intensity time series was no greater than 2 times that of the observational time series.

We run SIGMA over a uniformly sampled grid in the 4-D parametric space. We consider the range of *SpInd* from 0.6 to 6 while that of ΔN from 1.0e11 to 2.5e12 el/m³ for both altitudes. The discretization used in the simulation, which is primarily constrained by the computation time and resources, results in a resolution of $\delta SpInd = 0.6$ for *SpInd* and $\delta \Delta N \approx 2e11$ el/m³ for ΔN. Drift velocity magnitude and direction ranges are limited to ± 400 m/s and $\pm 30°$ about the estimated values obtained from SuperDARN mapped velocities. These have a step of 100 m/s and 10°, respectively. We do not expect to see any sharp gradients in the parametric space; however, since the function is nonlinear, there will always be an uncertainly associated with it. We find the global minimum value χ^2_{min}.

With an assumption that the measurement errors in the χ' minimization are normally distributed, we quantify the errors in the parameter estimation as described by *Press et al.* [1992]. The global minimum χ'_{min} is presented in the contour plots along with the confidence limits of 68.3% and 90% for that particular value. The confidence limits of 68.3% and 90% represent 1 and 2 standard deviation spread, respectively. We also specify the median value inside the 68.3% confidence contour.

To summarize, we use step 1 and step 2 from this section to solve the inverse modeling problem using SIGMA. We apply this technique to study the irregularities that produced the GPS scintillations at different locations shown in Figure 1. We present and discuss the results in the following section.

4. Results and Discussion

In this section, we describe the results of inverse modeling for one location, i.e., McMurdo in detail and briefly discuss the results of inverse modeling at the rest of the locations. The predictions of auroral oval boundaries from OVATION prime for both the hemispheres are shown in Figure 2. The station positions are highlighted
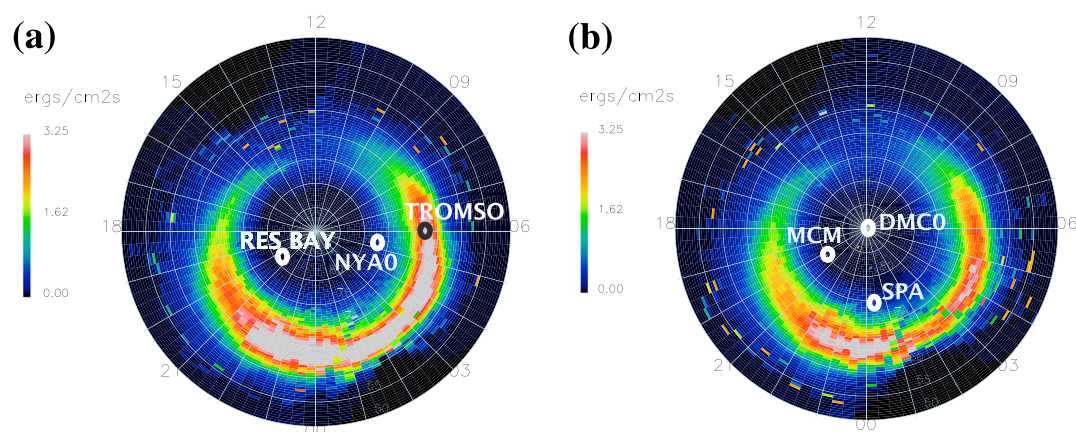
Figure 2. Forecast of (a) Northern auroral oval at 3:30 UT and (b) Southern auroral oval at 3:15 UT on 9 March 2012 displayed in magnetic local time and magnetic coordinate system. The yellow squares are the locations of GPS stations from where TEC measurements were obtained. Pink squares are radio occultations, and grey circles are SSUSI 1356 emissions.

on the plots. As seen from Figure 1, there are no periods of visible GPS scintillations over Concordia. The scintillations also get stronger as we go lower in the latitude. Using this observation and the auroral oval plots in Figure 2, we expect an absence of polar cap patches at higher latitudes, while at auroral and cusp stations, we believe that there is a good possibility of the scintillation occurrences being related to the auroral precipitation. In the following subsections, we describe the inverse modeling implementation and results. We also suggest some modifications to the technique for improved accuracy of the results.

4.1. McMurdo Results

From an inspection of the auroral oval boundaries in the Southern Hemisphere in Figure 2b, it is apparent that McMurdo was poleward of the auroral oval. In order to determine the altitude for the SIGMA simulation runs, we used IDA4D algorithm. The result of an IDA4D run over Antarctica is represented as a polar plot in Figure 3. It shows vertical total electron content (TEC) in geomagnetic coordinates. Since TEC maps have major
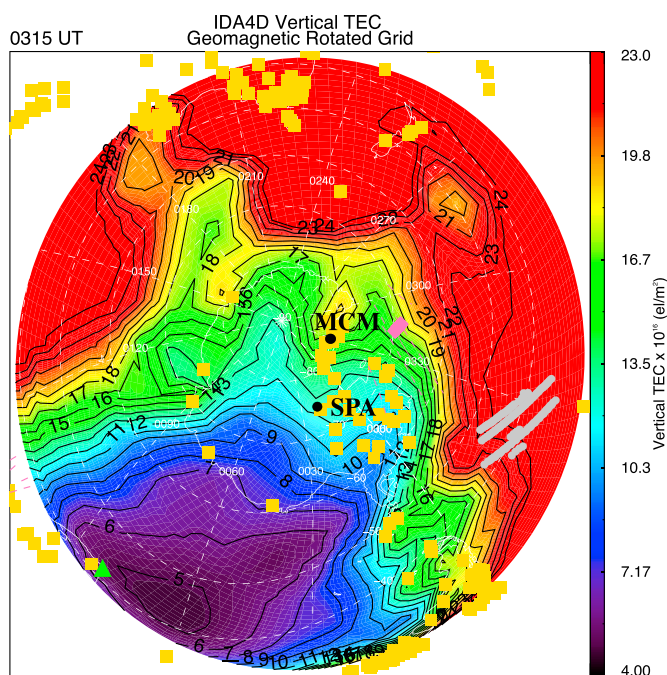

Figure 3. IDA4D polar plot displaying modeled vertical TEC in geomagnetic coordinates over Antarctica at 3:15 UT on 9 March 2012. The GPS station locations from where the TEC measurements were obtained are indicated in yellow squares.
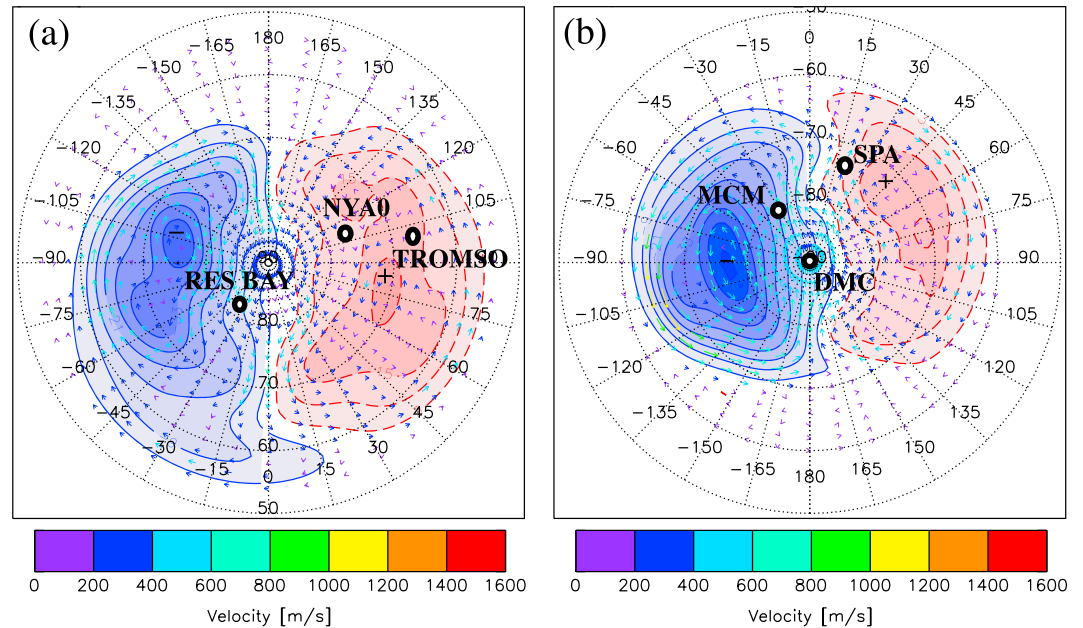
Figure 4. Convection velocity maps derived from SuperDARN data in (a) northern high-latitude region at 3:30 UT and (b) southern high-latitude region at 3:15 UT on 9 March 2012. The colored convection velocity vectors display the magnitudes based on the color bar.

contribution from *F* region, we think that this is a fair measure to understand the overall ionospheric structuring at around 350 km height. The plot shows some density enhancement over McMurdo. The scintillations could be the result of GPS signal passing through an *F* region irregularity of intermediate to medium scale size present in this enhanced-density region. However, taking a conservative approach, we solve the inverse problem at both *E* region and *F* region heights.

Figure 4 shows the SuperDARN convection velocity maps found using the technique described by *Ruohoniemi and Baker* [1998]. On 9 March 2012 close to 3:30 UT, the velocities over McMurdo are between 600 and 800 m/s at an azimuth of −110°. The azimuth defines the direction of $\mathbf{v}_d$, i.e., $\angle\mathbf{v}_d$, and is measured from the geomagnetic west direction. We note that these predictions are based on sparse E × B measurements from then available three Southern SuperDARN radars: Unwin (UNW), Kerguelen (KER), and Halley (HAL). Here we also remind that this is not the case for Northern Hemisphere that is well covered by SuperDARN radar observations. Therefore, the underlying convection model based on the interplanetary magnetic field B_z and B_y component values heavily influences the pattern in the south. Estimation of convection velocity using SuperDARN involves averaging; thus, the actual velocities could possibly be on the larger side, closer to 800 m/s at MCM. These drift velocity estimates from SuperDARN are only considered as starting predictions for unknown parameters (drift velocity magnitude and direction) while solving the inverse problem. Additionally, as explained in section 3.1, the drift velocity magnitude can also be estimated from the observed intensity PSD at MCM. These estimates are 800 m/s and 470 m/s with the assumed irregularity heights of 350 km and 120 km, respectively.

In Figure 5, we present the contours of χ' with respect to ΔN and *SpInd* at 120 km and 350 km heights and at the optimum velocity value. In other words, we obtain a 2-D slice of χ' at the optimum values of the magnitude and direction of $\mathbf{v}_d$. In all the contour plots, we show the positions of $\chi'_{\min}$, the median in the unit standard deviation spread. The two confidence levels are explained in section 3.2 and are indicated by dashed lines in this figure. For the 120 km case, we state that there is a 68.3% chance that the true values of ΔN and *SpInd* will fall within the region highlighted by 68.3% confidence level contour. It can also be seen that the 90% confidence level covers almost one third of the parametric space. Similarly, for 350 km case, the 90% confidence level covers almost the whole region. It should be noted that this solution is valid for a set of I_0, L_{Th} and AXR values. If there were a way to obtain the actual values of these three parameters from other sources, it would have been possible to obtain a better estimate of the unknowns. However, we can confidently
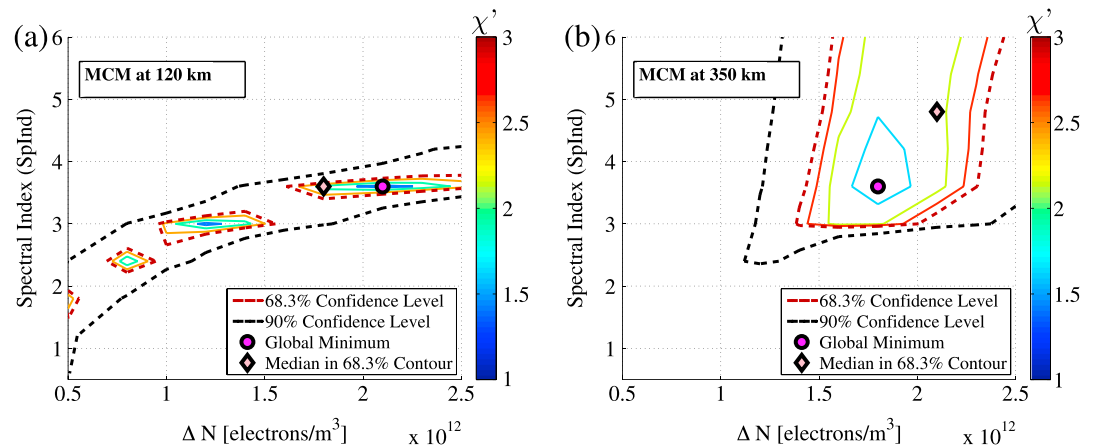
Figure 5. McMurdo case χ' contour plots showing different confidence levels at (a) 120 km and (b) 350 km. The color bars represent the values of χ'.

eliminate certain regions of the parametric space with this current method. For example, for the case of 120 km height, the region $\Delta N > 1e12$ el/m^3 and *SpInd* < 2 does not have an optimum solution.

We compare the observed and simulated PSDs with χ^2 fit. The global minimum value of χ' gives the simulated PSD that fits best to the observations. For this SIGMA simulation, we obtain the free parameter values and then plot the modeled and observed data in both the frequency and time domains. These are shown in Figure 6, where we compare the best fit SIGMA PSD against the observed PSD and also plot the best fit SIGMA phase time series with the observed phase time series at 120 km (Figures 6a and 6b) and 350 km (Figures 6c and 6d), respectively. The best fit simulated PSDs for 120 km and 350 km indeed appear to follow the observed PSD graph. A closer examination of the PSDs and the χ' values reveals that the SIGMA PSD at 120 km is a better fit to the observations compared with the 350 km case. We reiterate that if we try to fit the simulated time series to the observations instead of the PSDs, we would need to consider an extra free parameter or an unknown, that is, the time offset between the simulated and observed time series.

4.2. Inverse Modeling for MCM Case With Larger Thickness

In order to optimize the computational time for all the inverse modeling runs presented before, we initially had considered an irregularity thickness of 10 km at 350 km height, which is the same as that considered at 120 km height. However, in general, the expanse of irregularities at *F* region is expected to be larger than those at *E* region. In addition to the large-spread for *F* region irregularities, the *F* region has higher electron number density compared to the *E* region. These two factors call for a larger thickness for *F* region irregularities. Thus, we also solved the inverse modeling problem for each receiver location with an altitude of 350 km and a thickness of 40 km. The results of inverse modeling for MCM with larger thickness at *F* region altitude are displayed in Figure 7. It should be highlighted that the computational time and memory requirements of SIGMA increase nonlinearly as the thickness increases. The PSD of the best fit in Figure 7 shows a χ' value lower than that in Figures 6a and 6c. As mentioned in section 3.2, χ' value close to 1 indicates a good fit. Thus, χ' value from Figure 7a being very close to 1 compared with the higher χ' values from Figures 6a and 6c, proves that the best fit to McMurdo GPS scintillation observations occurs at 350 km altitude with $L_{Th} = 40$ km. Additionally, the best fit SIGMA phase time series displays comparable characteristics to the observed phase time series such as a period of oscillations of 5–7 s. From these observations it can be inferred that changing the thickness also affects some of the features in the PSD which in turn affects the fitting as well as some visually comparable details in the phase time series. Incorporating thickness as the fifth unknown parameter for the fitting function will be considered in future upgrades. This is because incorporating it in the inverse modeling optimization problem will require a consideration of multifold increase in the computational time which would in turn depend on the availability of higher-end computational resources. There has been a recent effort by *Chartier et al.* [2016] using a modified geometry inside SIGMA that attempts to accelerate its runs. Once it is validated with one of the inverse modeling runs, we plan to adopt it to be used in the standard inverse modeling analysis.
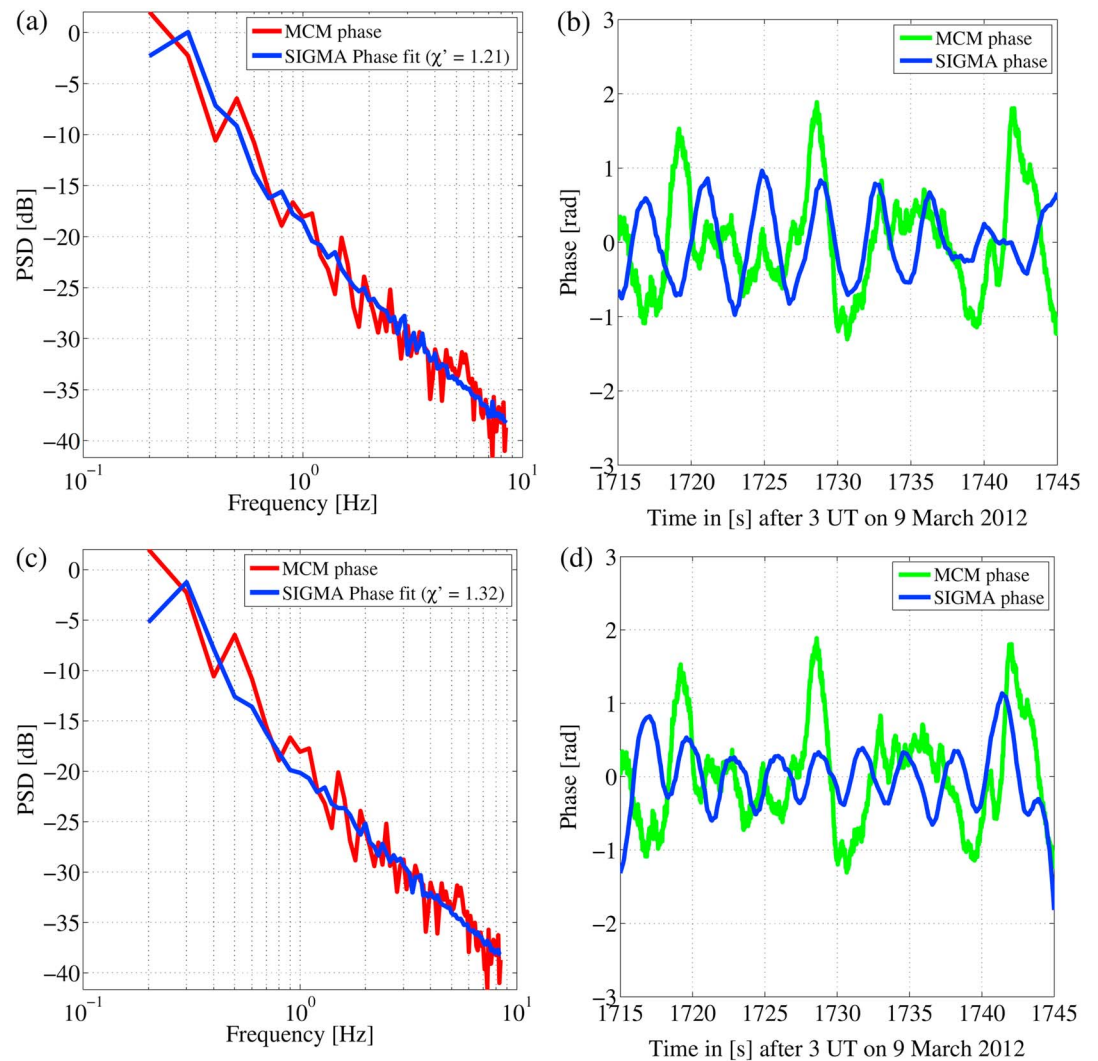
Figure 6. (a and c) PSD and (b and d) time series of the best fits for 120 km (Figures 6a and 6b) and 350 km (Figures 6c and 6d) heights at McMurdo.

4.3. Interpretation of Auxiliary Data for Remaining Stations

In order to estimate the height of the ionosphere related to the South Pole observations, we checked whether South Pole is under the auroral oval during the time of interest. From the modeled predictions of the auroral oval using OVATION Prime shown in Figure 2b, we see that South Pole is on the boundary of the auroral oval. Furthermore, the energetic particle precipitation data measured from the instrument SSUSI on board the DMSP F 18 satellite during the time 3:15 to 3:30 UT is plotted on the Antarctic map in Figure 8a. Although South Pole is not on the DMSP satellite path, it is certainly within $\approx 5°$ latitude from the path. With this in mind, one can see from Figure 8a that there is auroral precipitation close to South Pole. Moreover, from the keogram of imaging riometer at South Pole shown in Figure 8b, we can see a definite absorption around 3:10 to 3:20 UT. These evidences indicate that South Pole was inside the auroral oval or on its boundary. Thus, we propose that the GPS scintillations observed at South Pole are most likely related to an irregularity at E region height ($H_{iono} = 120$ km). The drift velocity at South Pole was estimated to be 400 m/s at an azimuth of $-110°$ from the SuperDARN plot in Figure 4b.

From Figure 2a, Tromsø clearly seems to be under the auroral oval indicating likeliness of presence of E region irregularities at 120 km height. The minimum RMS density variation over Tromsø was found to be 1e12 from ISR data. From the SuperDARN plot in Figure 4a, the velocity at Tromsø was deduced to be ≈ 400 m/s at an azimuth of 180°. For both SPA and Tromsø, we also solved SIGMA inverse modeling at F region height (with both 10 km and 40 km thick irregularities) and confirmed that the best fit indeed occurs at 120 km altitude.
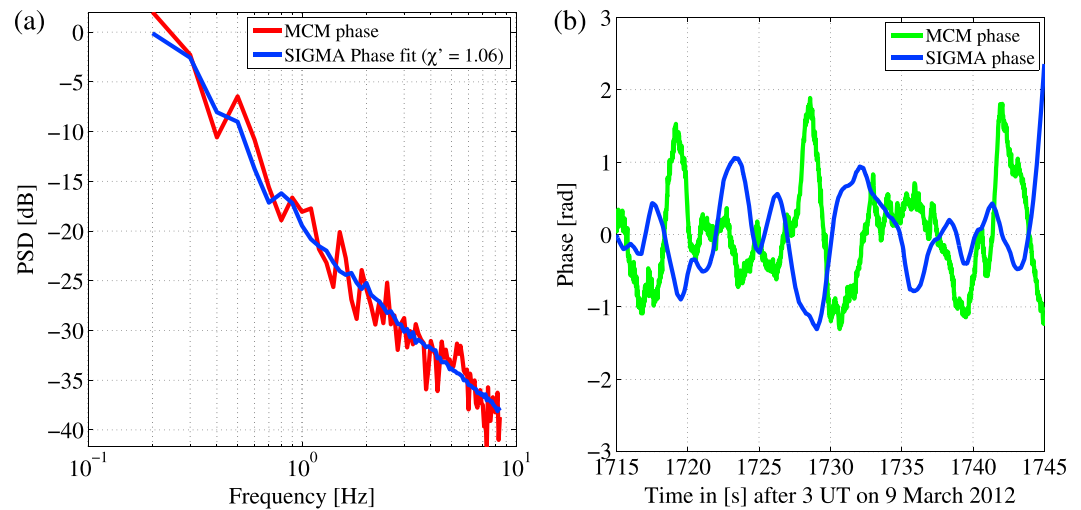
Figure 7. (a) PSD and (b) time series of the best fits for McMurdo with L_{Th} = 40 km thickness at 350 km height.

From Figure 2a Resolute Bay and Ny-Ålesund appear under the polar cap region. The estimated velocities at these two regions from the SuperDARN plot in Figure 4a are close to be 500 m/s and 200 m/s, respectively. The azimuths are 135° and −30°, respectively.

We found that the PSD of the best fit agreed with the observed PSD well for the case of 350 km altitude and 40 km thickness at Resolute Bay as well as Ny-Ålesund as shown in Figures 9a and 9c. Disregarding the time offset, the features (such as period of oscillation, peak to peak values) of the best fit simulated phase time series in Figures 9b and 9d appear to be consistent with those of the observed time series. The optimum parameter values for the SIGMA best fit for all the cases at each location are given in Table 3. The cases which we think fit the observations the best amongst all altitude and thickness combinations are shown in boldface. We would like to mention that a single-phase screen used in SIGMA represents an extended layer in altitude (40 km thick in F region case). We integrate along an oblique path while also considering the contribution from the horizontally nearby elements to the path and compute the phase fluctuations caused by the layer. So with SIGMA we consider the effect of field-aligned correlations of ionospheric irregularities.

4.4. Discussion of Inverse Modeling Results
From this work, our principal findings are as follows:

1. At all the considered high-latitude stations, we observed phase scintillations predominantly. The power shows only some small variations below the level of ±3 dB. At E and F regions, the predominance of phase
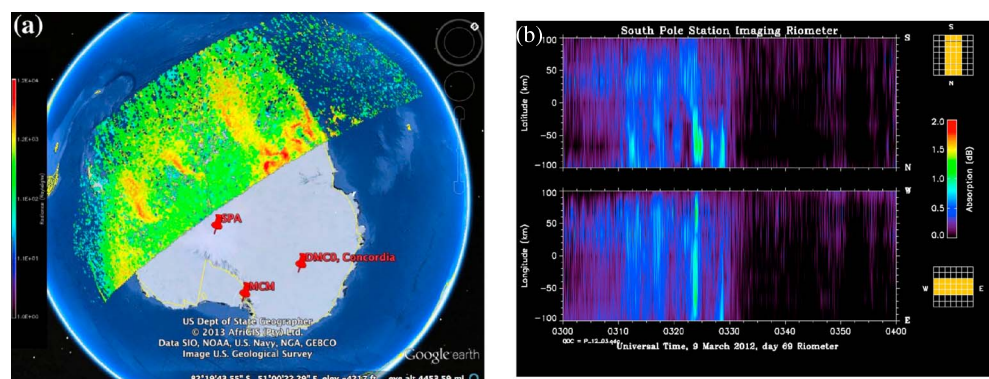

Figure 8. (a) Energetic particle precipitation over Antarctica from SSUSI instrument on the DMSP satellites and (b) Imaging riometer data at the South Pole displaying absorption around 3:15 UT, which most likely is due to energetic particle precipitation reaching the D region.
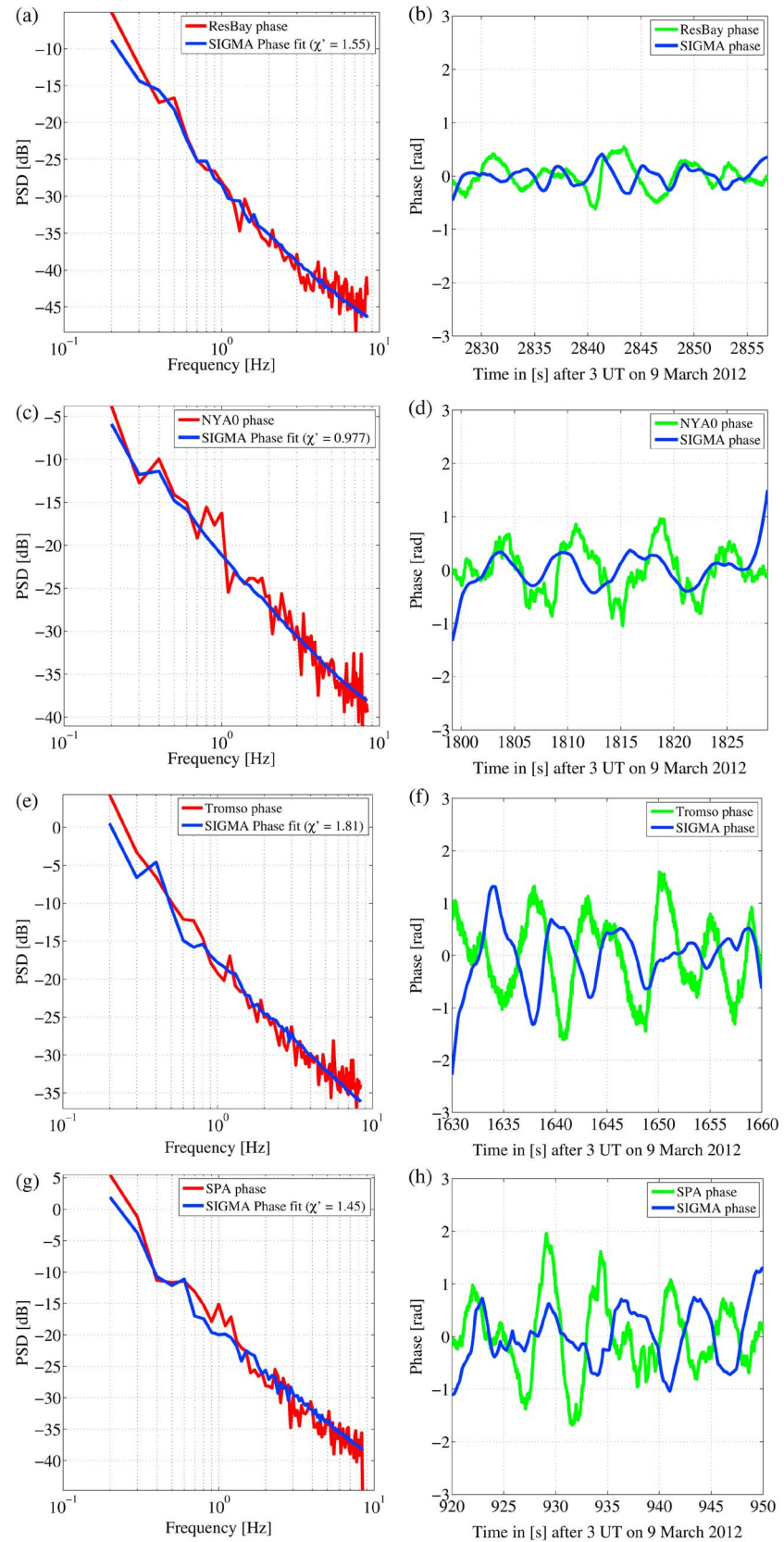
Figure 9. (a, c, e, and g) PSD and (b, d, f, and h) phase time series of the best fits for Resolute Bay (350 km), Ny-Ålesund (120 km), Tromsø (120 km), and SPA (120 km).

Table 3. SIGMA Optimum Parameter Values for Each Inverse Modeling Case at Different Locations[a]

SIGMA Parameters	l_0 (km)	SpInd	ΔN (el/m^3)	AXR	L_{Th} (km)	$|v_d|$ (m/s)	$\angle v_d$ (deg)	χ'
ResBay (at 120 km)	15	2.4	0.9e12	10	10	300	165	2.37
ResBay (at 350 km)	15	3.6	0.8e12	10	10	700	165	1.77
ResBay (at 350 km)	**15**	**3.6**	**0.6e12**	**10**	**40**	**550**	**157.5**	**1.55**
NYA0 (at 120 km)	15	3.0	1.0e12	10	10	450	−50	1.64
NYA0 (at 350 km)	15	2.4	1.0e12	10	10	400	−50	2.4
NYA0 (at 350 km)	**15**	**4**	**0.6e12**	**10**	**40**	**350**	**−37.5**	**0.98**
Tromsø (at 120 km)	**15**	**4.2**	**2.3e12**	**10**	**10**	**500**	**150**	**1.81**
Tromsø (at 350 km)	15	4.2	2.3e12	10	10	500	150	1.86
Tromsø (at 350 km)	15	5	0.6e12	10	40	500	150	1.9
SPA (at 120 km)	**15**	**2.4**	**1.0e12**	**10**	**10**	**400**	**−130**	**1.45**
SPA (at 350 km)	15	3.6	2.5e12	10	10	700	−110	1.32
SPA (at 350 km)	15	4	0.7e12	10	40	600	−140	1.54
MCM (at 120 km)	15	3.6	2.1e12	10	10	600	−110	1.21
MCM (at 350 km)	15	3.6	1.8e12	10	10	600	−100	1.32
MCM (at 350 km)	**15**	**4**	**0.3e12**	**10**	**40**	**800**	**−85**	**1.06**

[a]The cases which we found to be fitting the best to the observations for each receiver location are shown in boldface.

scintillations compared to amplitude scintillations indicates the presence of larger-scale irregularities of sizes above the Fresnel scale of hundred to a few hundred meters at GPS signal frequencies [*Yeh and Liu*, 1982].

2. The best fits from solving the inverse problem at different locations reveal that the spectral index of the irregularities varied between 2.4 and 4.2.

3. ΔN ranges from 0.3e12 to 2.3e12 el/m^3. Thus, considering respective irregularity thickness for each best fit, the turbulence strength in TECU ranges from 1 TECU to 2.4 TECU. These values are well within the limits seen in TEC maps in both the hemispheres during those times. However, it needs to be noted that TEC maps have very coarse resolution and have interpolated values at places where there are no measurements. The TEC enhancement of ∼18 TECU is seen over McMurdo in the IDA4D map. With the inverse method, we obtain the irregularity strength of about 1.2 TECU which is about 15% of the TEC enhancement and is consistent with our weak scattering assumption.

4. Altitudes of the irregularities responsible for scintillations were predicted from the model to be 350 km (*F* region) for McMurdo, Resolute Bay, and Ny-Ålesund, and 120 km (*E* region) for South Pole and Tromsø. Comparison with ionosonde data (if available) and/ or European Incoherent Scatter Scientific Association (EISCAT) radar would help in understanding the height at which ionospheric irregularities are located.

We report ambiguity surfaces in the parametric space of ΔN and *SpInd*, which are the result of uncertainty in the remaining input parameters. Availability of more auxiliary data would help eliminate these ambiguities. If a scintillation receiver records ΔTEC, it is possible to infer ΔN from that. Also, because of insufficient SuperDARN radar data coverage at high latitudes during the time of interest, there needs to be a more reliable source for obtaining the velocity estimates of intermediate and medium-scale irregularities. Localized spaced GPS scintillation receivers can provide accurate measurements of these drifts [*Bust et al.*, 2013; *Datta-Barua*, 2015].

Several experimental and modeling studies [*Basu et al.*, 1988; *Kelley et al.*, 1982b; *Keskinen and Ossakow*, 1982, 1983a; *Keskinen et al.*, 1988] have investigated the sources of high-latitude ionospheric irregularities. Reviews by *Keskinen and Ossakow* [1983b] and *Kintner and Seyler* [1985, and references therein] summarize the theories that explain the origin of these irregularities. *Tsunoda* [1988] found that E × B (gradient drift) instability is the dominant mechanism in the the *F* region polar ionosphere. In situ satellite measurements and scintillation measurements reported a spectral index $m \leq 2$ for *F* region irregularities [*Basu et al.*, 1988]. Additionally, non-linear evolution of the Kelvin-Helmholtz instability at high latitudes studied by *Keskinen et al.* [1988] revealed the spectral indices of transverse averaged power spectra of density in the range of 1.6 ± 0.2 to 2.2 ± 0.2 depending on whether collisional effects are important. These spectra are one-dimensional (1-D). In situ

measurements from probes on board satellites also yield spectral index for a 1-D power law irregularity spectrum. Thus, for 1-D spectral index m close to 2 (from the in situ measurements, etc.) the spectral index p must be close to 4 for a 3-D spectrum [*Yeh and Liu*, 1982]. The spectral index values we obtained from our inverse modeling of our F region fits (found using a 3-D hybrid spectrum) are 3.6 and 4, which are thus close to this expected value of $p \sim 4$.

Keskinen and Ossakow [1983b] mention that strong electrojet currents across geomagnetic field in the high-latitude E region are believed to be the drivers of Farley-Buneman (two stream) and E × B instabilities. Farley-Buneman instability is driven by an electrojet current that may be responsible for small-scale (wavelengths less than 10 km) irregularities, while large-scale (wavelengths greater than 10 km) irregularities may be produced by the E × B instability. For Tromsø and South Pole, where the best fits appear at E region altitudes, the spectral index values for the electron number density spectra are 4.2 and 2.4, respectively. Previous work by *Oppenheim and Otani* [1996] address the spectral characteristics of Farley-Buneman instabilities at low latitudes, but there needs to be more work done on these instabilities at high latitudes. Due to lack of theoretical spectral studies of E region irregularities at high latitudes, it is hard to determine the type of instability based on the spectral indices. However, we believe that E region irregularities responsible for the GPS scintillations observed at Tromsø and South Pole are result of soft auroral precipitation and thus most likely are associated with two-stream instability.

We would like to state that while using such an inverse method, a few discrepancies in finding the best fit may arise because of lack of information about the measurement errors. For higher fidelity, we require better estimate of measurement errors. The disagreement, if any, between the best fit SIGMA PSD and observed PSD, could occur because of the following possibilities. First, there is insufficient information to find actual values of some inputs from auxiliary data. Second, the underlying spectral model with a single-slope power law is inadequate to describe the physics of the irregularities involved in those observations.

5. Conclusion and Future Work

The characterization of ionospheric irregularities is important to further our understanding of the underlying physics and also in mitigation of the scintillation effects in the GNSS signals. We use an inverse modeling technique with the help of a global scintillation model SIGMA to characterize the intermediate-scale (0.1 – 10 km) to medium-scale (10 – 100 km) high-latitude irregularities which are likely to produce ionospheric scintillations in the GNSS signals. In this investigation, we consider ground observations from both the northern and southern high latitudes during a geomagnetically active period on 9 March 2012. We compare the high-rate GPS observations to the SIGMA model predictions and using the inverse method derive some of the physical properties of the irregularities. According to our knowledge, high-rate GPS data along with a model comparison have never been utilized in high-latitude interhemispheric studies. For our inverse method, we initially use available auxiliary data to deduce some of the input parameters of SIGMA for a given GNSS observation. Subsequently, for each observation, we obtain optimal values of the remaining unknown SIGMA parameters. The SIGMA input parameters thus derived represent the physical and propagation parameters related to the physics of the irregularity that produced those GNSS scintillations.

The results indicate that the spectral index ranges from 2.4 to 4.2. For F region irregularities the values are close to 4, which is consistent with the theoretical expectation for 3-D irregularity spectra. The RMS number density ranges from 3e11 to 2.3e12 el/m^3. The turbulence strength in TEC ranges from 1 TECU to 2.4 TECU. These TECU values were found to be within the observed limits in TEC maps in both the hemispheres during those times. The best fits we obtained from our inverse method that considers only weak scattering mostly agree with the observations and indicated irregularity altitudes of 120 km (E region) and 350 km (F region) at the auroral or cusp and polar cap locations, respectively. Finally, predominance of phase scintillations compared to amplitude scintillations at these high latitudes imply the presence of larger-scale irregularities of sizes above the Fresnel scale of hundred to a few hundred meters at GPS signal frequencies.

The best fits we obtained from our inverse method mostly agree with the observations, but we also report important discrepancies. These discrepancies in obtaining a unique solution could be reduced with the availability of more auxiliary data and better estimates of the measurement errors. The inverse modeling technique can be refined by implementing our recommendations from this study especially like implementing larger or variable thickness option in the inverse modeling optimization problem. Inverse modeling using more than

four unknowns, variable thickness, a generalized spectral model of high-latitude irregularities, global optimization algorithm, and a modification in the geometry of the electron density distribution in SIGMA are future advancements in the current methodology. In addition to these, we will include the option of increasing the number of layers as a standard part of inverse modeling analysis. Although some of these changes may add multifold computational challenges to the current work, we plan to pursue them as follow-up research. We believe that with some upgrades, this inverse modeling technique will be instrumental in routinely deriving the physics of the ionospheric irregularities from GNSS observations.

References

Aarons, J. (1982), Global morphology of ionospheric scintillations, *IEEE Proc.*, *70*, 360–378.

Aarons, J. (1997), Global positioning system phase fluctuations at auroral latitudes, *J. Geophys. Res.*, *102*, 17,219–17,232, doi:10.1029/97JA01118.

Alfonsi, L., L. Spogli, G. De Franceschi, V. Romano, M. Aquino, A. Dodson, and C. N. Mitchell (2011), Bipolar climatology of GPS ionospheric scintillation at solar minimum, *Radio Sci.*, *46*, RS0D05, doi:10.1029/2010RS004571.

Basu, S., E. MacKenzie, S. Basu, P. F. Fougere, N. C. Maynard, W. R. Coley, W. B. Hanson, J. D. Winningham, M. Sugiura, and W. R. Hoegy (1988), Simultaneous density and electric field fluctuation spectra associated with velocity shears in the auroral oval, *J. Geophys. Res.*, *93*, 115–136, doi:10.1029/JA093iA01p00115.

Basu, S., E. J. Weber, T. W. Bullett, M. J. Keskinen, E. MacKenzie, P. Doherty, R. Sheehan, H. Kuenzler, P. Ning, and J. Bongiolatti (1998), Characteristics of plasma structuring in the cusp/cleft region at Svalbard, *Radio Sci.*, *33*, 1885–1900, doi:10.1029/98RS01597.

Bust, G., S. Datta-Barua, K. Deshpande, S. Bourand, S. Skone, and Y. Su (2013), Correlation properties of a 2-D array of high latitude scintillation receivers, paper presented at 26th International Technical Meeting of The Satellite Division of the Institute of Navigation (ION GNSS 2013), pp. 2470–2479, Nashville, Sept. 2013.

Bust, G. S., and S. Datta-Barua (2014), *Scientific Investigations Using IDA4D and EMPIRE*, pp. 283–297, John Wiley, New York.

Bust, G. S., T. W. Garner, and T. L. Gaussiran (2004), Ionospheric Data Assimilation Three-Dimensional (IDA3D): A global, multisensor, electron density specification algorithm, *J. Geophys. Res.*, *109*, A11312, doi:10.1029/2003JA010234.

Carrano, C. S., C. E. Valladares, and K. M. Groves (2012), Latitudinal and local time variation of ionospheric turbulence parameters during the conjugate point equatorial experiment in Brazil, *Int. J. Geophys.*, *2012*, 103963, doi:10.1155/2012/103963.

Chartier, A., B. Forte, K. Deshpande, G. Bust, and C. Mitchell (2016), Three-dimensional modeling of high-latitude scintillation observations, *Radio Sci.*, *51*, 1022–1029, doi:10.1002/2015RS005889.

Chernoff, H., and E. L. Lehmann (1954), The use of maximum likelihood estimates in x^2 tests for goodness of fit, *Ann. Math. Stat.*, *25*(3), 579–586, doi:10.1214/aoms/1177728726.

Costa, E., and M. C. Kelley (1977), Ionospheric scintillation calculations based on in situ irregularity spectra, *Radio Sci.*, *12*, 797–809, doi:10.1029/RS012i005p00797.

Datta-Barua, S., Y. Su, K. Deshpande, D. Miladinovich, G. S. Bust, D. Hampton, and G. Crowley (2015), First light from a kilometer-baseline Scintillation Auroral GPS Array, *Geophys. Res. Lett.*, *42*, 3639–3646, doi:10.1002/2015GL063556.

Deshpande, K. B., G. S. Bust, C. R. Clauer, H. Kim, J. E. Macon, T. E. Humphreys, J. A. Bhatti, S. B. Musko, G. Crowley, and A. T. Weatherwax (2012), Initial GPS Scintillation results from CASES receiver at South Pole, Antarctica, *Radio Sci.*, *47*, RS5009, doi:10.1029/2012RS005061.

Deshpande, K. B., G. S. Bust, C. R. Clauer, C. L. Rino, and C. S. Carrano (2014), Satellite-beacon Ionospheric-scintillation Global Model of the upper Atmosphere (SIGMA) I: High latitude sensitivity study of the model parameters, *J. Geophys. Res. Space Physics*, *119*, 4026–4043, doi:10.1002/2013JA019699.

Jayachandran, P. T., et al. (2009), Canadian High Arctic Ionospheric Network (CHAIN), *Radio Sci.*, *44*, RS0A03, doi:10.1029/2008RS004046.

Kelley, M. C., R. Pfaff, K. D. Baker, J. C. Ulwick, R. Livingston, C. Rino, and R. Tsunoda (1982a), Simultaneous rocket probe and radar measurements of equatorial spread F—Transitional and short wavelength results, *J. Geophys. Res.*, *87*, 1575–1588, doi:10.1029/JA087iA03p01575.

Kelley, M. C., J. F. Vickrey, C. W. Carlson, and R. Torbert (1982b), On the origin and spatial extent of high-latitude F region irregularities, *J. Geophys. Res.*, *87*, 4469–4475, doi:10.1029/JA087iA06p04469.

Keskinen, M. J. (2006), GPS scintillation channel model for the disturbed low-latitude ionosphere, *Radio Sci.*, *41*, RS4003, doi:10.1029/2005RS003442.

Keskinen, M. J., and S. L. Ossakow (1982), Nonlinear evolution of plasma enhancements in the auroral ionosphere. I—Long wavelength irregularities, *J. Geophys. Res.*, *87*, 144–150, doi:10.1029/JA087iA01p00144.

Keskinen, M. J., and S. L. Ossakow (1983a), Nonlinear evolution of convecting plasma enhancements in the auroral ionosphere. II—Small scale irregularities, *J. Geophys. Res.*, *88*, 474–482, doi:10.1029/JA088iA01p00474.

Keskinen, M. J., and S. L. Ossakow (1983b), Theories of high-latitude ionospheric irregularities: A review, *Radio Sci.*, *18*, 1077–1091, doi:10.1029/RS018i006p01077.

Keskinen, M. J., H. G. Mitchell, J. A. Fedder, P. Satyanarayana, and S. T. Zalesak (1988), Nonlinear evolution of the Kelvin-Helmholtz instability in the high-latitude ionosphere, *J. Geophys. Res.*, *93*, 137–152, doi:10.1029/JA093iA01p00137.

Kinrade, J., C. N. Mitchell, P. Yin, N. Smith, M. J. Jarvis, D. J. Maxfield, M. C. Rose, G. S. Bust, and A. T. Weatherwax (2012), Ionospheric scintillation over Antarctica during the storm of 5–6 April 2010, *J. Geophys. Res.*, *117*, A05304, doi:10.1029/2011JA017073.

Kinrade, J., C. N. Mitchell, N. D. Smith, Y. Ebihara, A. T. Weatherwax, and G. S. Bust (2013), GPS phase scintillation associated with optical auroral emissions: First statistical results from the geographic South Pole, *J. Geophys. Res. Space Physics*, *118*, 2490–2502, doi:10.1002/jgra.50214.

Kintner, P. M., and C. E. Seyler (1985), The status of observations and theory of high latitude ionospheric and magnetospheric plasma turbulence, *Space Sci. Rev.*, *41*, 91–129, doi:10.1007/BF00241347.

Kintner, P. M., T. Humphreys, and J. Hinks (2009), Gnss and ionospheric scintillation, *Inside GNSS*, *4*(4), 22–30.

Machol, J. L., J. C. Green, R. J. Redmon, R. A. Viereck, and P. T. Newell (2012), Evaluation of ovation prime as a forecast model for visible aurorae, *Space Weather*, *10*, S03005, doi:10.1029/2011SW000746.

Mitchell, C. N., L. Alfonsi, G. De Franceschi, M. Lester, V. Romano, and A. W. Wernik (2005), GPS TEC and scintillation measurements from the polar ionosphere during the October 2003 storm, *Geophys. Res. Lett.*, *32*, L12S03, doi:10.1029/2004GL021644.

Newell, P. T., T. Sotirelis, and S. Wing (2009), Diffuse, monoenergetic, and broadband aurora: The global precipitation budget, *J. Geophys. Res.*, *114*, A09207, doi:10.1029/2009JA014326.

Newell, P. T., T. Sotirelis, and S. Wing (2010), Seasonal variations in diffuse, monoenergetic, and broadband aurora, *J. Geophys. Res.*, *115*, A03216, doi:10.1029/2009JA014805.

Oppenheim, M., and N. Otani (1996), Spectral characteristics of the farley-buneman instability: Simulations versus observations, *J. Geophys. Res.*, *101*(A11), 24,573–24,582, doi:10.1029/96JA02237.

Paxton, L. J., D. Morrison, Y. Zhang, H. Kil, B. Wolven, B. S. Ogorzalek, D. C. Humm, and C.-I. Meng (2002), Validation of remote sensing products produced by the Special Sensor Ultraviolet Scanning Imager (SSUSI): A far UV-imaging spectrograph on DMSP F-16, *Proc. SPIE*, *4485*, 338–348, doi:10.1117/12.454268.

Press, W., B. Flannery, S. Teukolsky, and W. Vetterling (1992), *Numerical Recipes in C: The Art of Scientific Computing*, Cambridge Univ. Press, Cambridge, U. K.

Prikryl, P., P. T. Jayachandran, S. C. Mushini, D. Pokhotelov, J. W. MacDougall, E. Donovan, E. Spanswick, and J.-P. St.-Maurice (2010), GPS TEC, scintillation and cycle slips observed at high latitudes during solar minimum, *Ann. Geophys.*, *28*, 1307–1316, doi:10.5194/angeo-28-1307-2010.

Prikryl, P., et al. (2011), Interhemispheric comparison of GPS phase scintillation at high latitudes during the magnetic-cloud-induced geomagnetic storm of 5–7 April 2010, *Ann. Geophys.*, *29*, 2287–2304, doi:10.5194/angeo-29-2287-2011.

Prikryl, P., P. T. Jayachandran, S. C. Mushini, and I. G. Richardson (2012), Toward the probabilistic forecasting of high-latitude GPS phase scintillation, *Space Weather*, *10*, S08005, doi:10.1029/2012SW000800.

Prikryl, P., et al. (2015), GPS phase scintillation at high latitudes during geomagnetic storms of 7–17 March 2012 Part 2: Interhemispheric comparison, *Ann. Geophys.*, *33*(6), 657–670, doi:10.5194/angeo-33-657-2015.

Rino, C. L. (1979), A power law phase screen model for ionospheric scintillation. I—Weak scatter, *Radio Sci.*, *14*, 1135–1145, doi:10.1029/RS014i006p01135.

Rino, C. L. (2010), *The Theory of Scintillation with Applications in Remote Sensing*, John Wiley, New York.

Rino, C. L., and C. S. Carrano (2011), The application of numerical simulations in Beacon scintillation analysis and modeling, *Radio Sci.*, *46*, RS0D02, doi:10.1029/2010RS004563.

Rino, C. L., and E. J. Fremouw (1977), The angle dependence of singly scattered wavefields, *J. Atmos. Terr. Phys.*, *39*, 859–868.

Romano, V., S. Pau, M. Pezzopane, E. Zuccheretti, B. Zolesi, G. De Franceschi, and S. Locatelli (2008), The electronic Space Weather upper atmosphere (eSWua) project at INGV: Advancements and state of the art, *Ann. Geophys.*, *26*(2), 345–351, doi:10.5194/angeo-26-345-2008.

Romano, V., S. Pau, M. Pezzopane, L. Spogli, E. Zuccheretti, M. Aquino, and C. Hancock (2013), eSWua: A tool to manage and access GNSS ionospheric data from mid-to-high latitudes, *Ann. Geophys.*, *56*(2), R0223, doi:10.4401/ag-6244.

Ruohoniemi, J. M., and K. B. Baker (1998), Large-scale imaging of high-latitude convection with Super Dual Auroral Radar Network HF radar observations, *J. Geophys. Res.*, *103*, 20,797–20,811, doi:10.1029/98JA01288.

Spencer, P. S. J., and C. N. Mitchell (2007), Imaging of fast moving electron-density structures in the polar cap, *Ann. Geophys.*, *50*, 427–434.

Spogli, L., L. Alfonsi, G. de Franceschi, V. Romano, M. H. O. Aquino, and A. Dodson (2009), Climatology of GPS ionospheric scintillations over high and mid-latitude European regions, *Ann. Geophys.*, *27*, 3429–3437, doi:10.5194/angeo-27-3429-2009.

Tsunoda, R. T. (1988), High-latitude F region irregularities—A review and synthesis, *Rev. Geophys.*, *26*, 719–760, doi:10.1029/RG026i004p00719.

Van Dierendonck, A. J., J. Klobuchar, and Q. Hua (1993), Ionospheric scintillation monitoring using commercial single frequency C/A code receivers, paper presented at 6th International Technical Meeting of the Satellite Division of The Institute of Navigation (ION GPS 1993), pp. 1333–1342, Salt Lake City, UT, Sept. 1993.

Welch, P. D. (1967), The use of fast fourier transform for the estimation of power spectra: A method based on time averaging over short, modified periodograms, *IEEE Trans. Audio Electroacoust.*, *15*(2), 70–73, doi:10.1109/TAU.1967.1161901.

Wernik, A. W., L. Alfonsi, and M. Materassi (2007), Scintillation modeling using in situ data, *Radio Sci.*, *42*, RS1002, doi:10.1029/2006RS003512.

Yeh, K. C., and C.-H. Liu (1982), Radio wave scintillations in the ionosphere, *IEEE Proc.*, *70*, 324–360.

Zhang, Y., and L. Paxton (2008), An empirical Kp-dependent global auroral model based on TIMED/GUVI FUV data, *J. Atmos. Sol. Terr. Phys.*, *70*(8–9), 1231–1242, doi:10.1016/j.jastp.2008.03.008.